

Emerging negative Poisson's ratio driven by strong intralayer interaction response in rectangular transition metal chalcogenides

Linfeng Yu¹, Yancong Wang¹, Xiong Zheng¹, Huimin Wang², Zhenzhen Qin³, and Guangzhao Qin^{1,*}

¹*State Key Laboratory of Advanced Design and Manufacturing for Vehicle Body, College of Mechanical and Vehicle Engineering, Hunan University, Changsha 410082, P. R. China*

²*Hunan Key Laboratory for Micro-Nano Energy Materials & Device and School of Physics and Optoelectronics, Xiangtan University, Xiangtan 411105, Hunan, China*

³*School of Physics and Microelectronics, Zhengzhou University, Zhengzhou 450001, China*

Abstract

Auxetic behavior quantified by the negative Poisson's ratio (NPR) is commonly attributed to geometry evolution with re-entrant mechanism or other mechanical factors, which is thought to be independent of electronic structures. Thus, searching for electronic effect dominated auxetic behavior is challenging. Herein, from *state-of-the-art* first-principles calculations, by studying a class of two-dimensional (2D) transition metal chalcogenides (TMCs), namely X_2Y_2 -type ($X=Cu, Ag, Au$; $Y=O, S, Se$) rectangular TMCs (R-TMCs), we identify that the monolayer R-Cu₂Se₂ unconventionally demonstrates a structure-independent anisotropic NPR. In contrast, the NPR is absent in other R-TMCs. The emerging NPR is attributed to the strong strain response of intralayer interaction in R-Cu₂Se₂, which can be traced to the lone pair electrons and weak electronegativity of Se atoms under multi-orbital hybridization. The emerging NPR would make R-Cu₂Se₂ a promising candidate in electronics protection, and our study would provide valuable clues and useful guidance for designing advanced auxetic materials.

Keywords: negative Poisson's ratio, R-TMCs, R-Cu₂Se₂, transition metal chalcogenide, first-principles calculations

* Author to whom all correspondence should be addressed. E-Mail: gzqin@hnu.edu.cn

1. Introduction

The last years have witnessed the prosperity of auxetic materials. As a functional mechanical phenomenon, auxetic effect means that a material expands (contracts) when it is stretched (compressed) *i.e.* negative Poisson's ratio (NPR). Auxetic materials have excellent mechanical properties such as enhanced toughness, shear resistance and vibration absorption¹. Hence, they has greatly potential applications in medicine, defense, tougher composites and other broad fields²⁻⁴. In classical elastic theory, Poisson's ratio ranges from -0.5 to 1⁵, and then the NPR is theoretically reasonable in three-dimensional (3D) continuous materials like bulk auxetic structures^{6,7} and metals^{8,9}. With the explosion of two-dimensional (2D) materials, the excellent properties of 2D materials have been driving its rapid development. Outstanding representatives include graphene-like materials¹⁰⁻¹³, transition metal chalcogenides (TMCs)¹⁴⁻¹⁶, and transition metal halide¹⁷⁻¹⁹ *etc.* it is expected to find this novel NPR phenomenon in 2D materials.

The intrinsic NPR in 2D materials refers to the auxetic effect that manifests without external influence, which can be divided into five behaviors²⁰ as follows: (1) *In-plane* NPR behavior; (2) *Out-of-plane* NPR behavior; (3) Bidirectional NPR behavior; (4) *In-plane* half-NPR behavior²¹; (5) *Out-of-plane* half-NPR behavior. However, most 2D materials tend to have a positive Poisson's ratio (PPR), and their NPR must be activated by external techniques. For instance, the NPR in 2D graphene-like compound^{22,23,24} can be activated through strain engineering. In addition, oxidation²⁵, vacancy defects²⁶, and cutting into nanoribbons²⁷ are also reported to activate NPR. In recent years, many efforts have been devoted to searching for intrinsic NPR in 2D materials based on specific lattice structure, including puckered -materials^{28,29}, square-materials^{15,30}, and other configurations^{21,31-33}. However, the origin of intrinsic NPRs is usually attributed to the unique geometric structures with a re-entrant mechanism or other mechanical factor, regardless of its electronic properties. For instance, the NPR of puckered materials such as black phosphorene originates from the re-entrant mechanism^{28,29}, and the recently reported NPR of wurtzite monolayers originates from the folded in-plane triangular stacking³⁴. Distinct from above auxetic materials, an unusual NPR behavior dominated by electronic effects is found in 1T-TMCs³⁵ by *Yu et al* inadvertently in the form of filled electron orbitals. Combined with other remarkable properties of such NPR materials could lead to unexpected multi-functionalities. Since then, there is no similar NPR materials dominated by electronic effects has been found in any other configuration and the lack of cases provides poor insight into this unique behavior, which arise a thought-provoking question whether there are other special NPR mechanisms beyond 1T-TMCs or any auxetic configurations without re-entrant.

In this study, we report a novel 2D TMCs with intrinsic NPR behavior based on first-principles methods. The difference from other reported auxetic materials lies in their mechanical structure and more in the microscopic origin of their Poisson's ratio behavior. All TMCs monolayers are of rectangular X_2Y_2 type ($X=Cu, Ag, Au$ and $Y=O, S, Se$), named $R-X_2Y_2$. Most importantly, a structure-independent NPR behavior is

found in monolayer R-Cu₂Se₂. Unlike previously reported NPRs dominated by re-entrant mechanisms, such behavior cannot gain insight from geometric behavior because while other R-X₂Y₂ configurations are not found. This emerging NPR in R-X₂Y₂ monolayers can be explained by their distinct response strength of intralayer interactions. In addition, the stability of R-X₂Y₂ monolayers is confirmed to be dynamically, thermally and mechanically stable and they exhibit promising electrically semiconducting and optical absorption properties. Auxetic properties combined with these promising optical and electrical properties. properties make R-TMCs a promising candidate for protecting electronics.

2. Results and discussion

2.1. Structure of R-X₂Y₂ and the stability verification

As shown in Fig. 1(a), the primitive cell of R-X₂Y₂ monolayers contains two X (X=Cu, Ag and Au) atoms and two Y (Y=O, S and Se) atoms, which is different from XY₂-type 1T (or 2H)-TMCs. From the side view, R-X₂Y₂ monolayers have a zigzag-shaped washboard configuration, and they do not exhibit mirror symmetry (like 2H-TMCs) but centrosymmetric (like 1T-TMCs). Interestingly, R-X₂Y₂ monolayers inherit the non-metal shielding properties in traditional TMCs (1T and 2H phase), namely, the metal X atoms are in the middle layer and the non-metal Y atoms are in the outer layer. In addition, the X atom in the middle of the layer forms a two- and four-coordinate bonding configuration with the Y atom, respectively, while the two Y atoms only form an equivalent three-coordinate configuration. Fig. 1(b) further demonstrates the localized symmetric atomic schematic involving NPR evolution. The labels a , b , h and θ represent the lattice constant along the x and y directions, the buckling height and characteristic angle, respectively, which are listed in Table 1. The unique buckling structure reduces atomic Y-Y repulsion, and thus R-X₂Y₂ may be relatively stable.

The stability of R-X₂Y₂ monolayers can be confirmed based on phonon dispersion as shown in the supplementary Fig. S1, which reflects the dynamic stability of the system. Considering that the NPR only appears in monolayer R-Cu₂Se₂, we only focus on the results of monolayer R-Cu₂Se₂. The phonon dispersion of monolayer R-Cu₂Se₂ is plotted in Fig. 1(c), where no imaginary frequencies appear in the acoustic phonon branch. Thus, monolayer R-Cu₂Se₂ is dynamically stable. Furthermore, *ab initio molecular dynamics* (AIMD)^{36,37} simulations are performed to assess thermal stability, which are shown in the supplementary Fig. S2. The stable temperature distribution at 300 K and a snapshot of the configuration after the AIMD simulation indicate its stability in room temperature. Mechanically, the stability of monolayer R-Cu₂Se₂ need to meet the Born–Huang criteria³⁸, *i.e.*, C_{11} , C_{12} , $C_{66} > 0$ and $C_{11}+C_{22} > 2C_{12}$, where C_{ij} represents elastic constant. The calculated values of C_{11} , C_{22} , C_{12} , and C_{66} of R-X₂Y₂ monolayers are listed in Table 1, which satisfy mechanical stability. Noted that the C_{11} , C_{22} , C_{12} , and C_{66} of 38.27, 2.88, -0.71 and 0.84 N/m for monolayer R-Cu₂Se₂

satisfies the criteria. These results strongly demonstrate the stability of monolayer R-Cu₂Se₂. More mechanical information is found in Supplementary NoteS1, Table S1 and Fig S4.

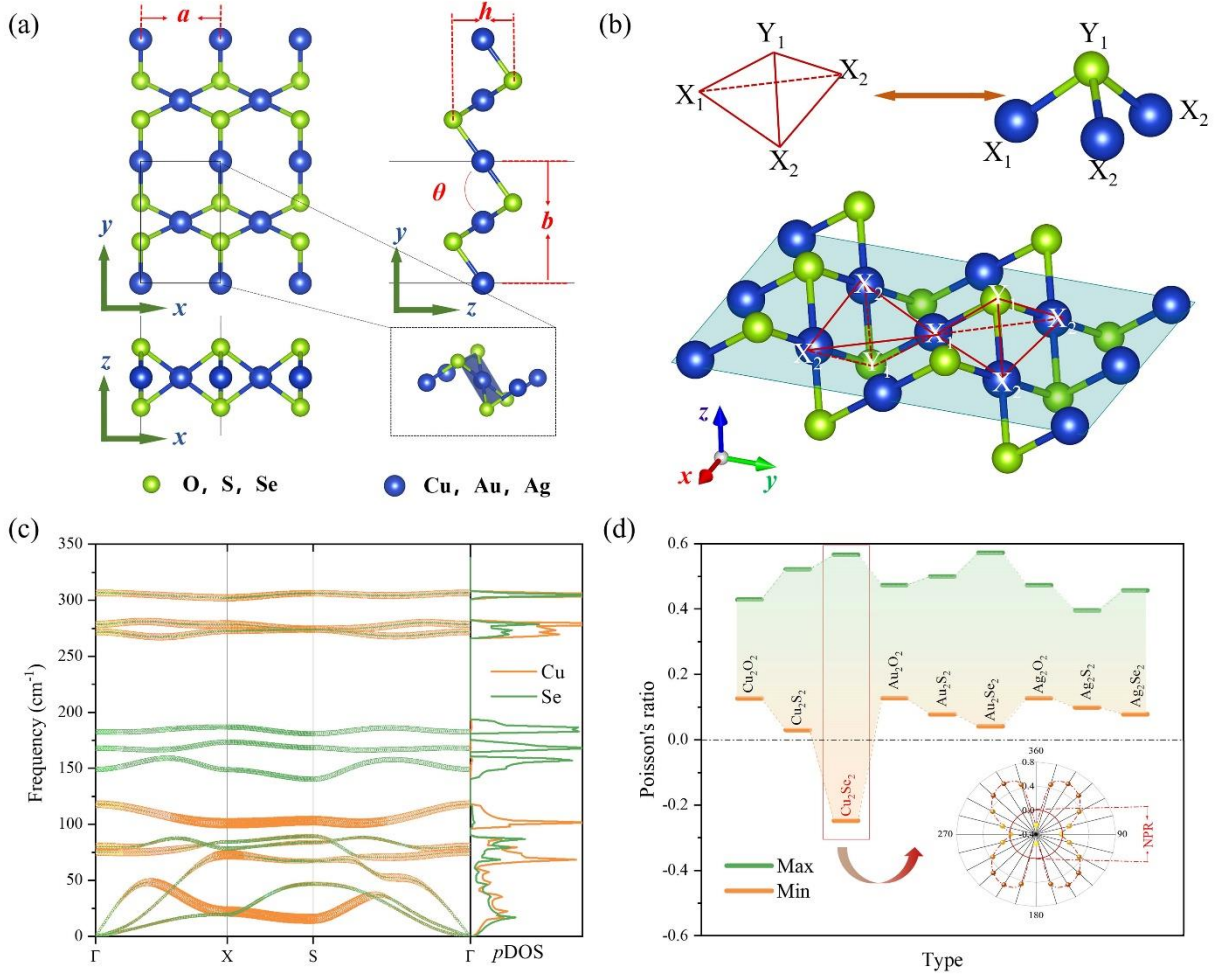


Figure 1. (a) The views of the geometry structures of R- X₂Y₂ (X=Cu, Ag, Au and Y=O, S, Se). The gray dashed line marks the crystal lattice. (b) Local lattice morphology and atoms with symmetrical motion in R- X₂Y₂. (c) Phonon dispersion and partial density of states (*pDOS*) of monolayer R-Cu₂Se₂ with spitted contribution from different atoms. (d) The highest and lowest Poisson's ratio of R-X₂Y₂ monolayers. The inset shows the direction dependence of Poisson's ratio for monolayer R-Cu₂Se₂.

Table 1. Comparison of basic physical properties for R-X₂Y₂ (X=Cu, Ag, Au; Y=O, S, Se) monolayers. Lattice constant *a*, *b*; Buckling height *h*; Characteristic angle *θ*; Band gap from HSE06 (*E*_{HSE06}) and PBE (*E*_{PBE}) functionals; Elastic constant *C_{ij}* (*i*, *j*=1, 2, 6).

	<i>a</i> (Å)	<i>b</i> (Å)	<i>h</i> (Å)	<i>θ</i> (°)	<i>E</i> _{HSE06} (eV)	<i>E</i> _{PBE} (eV)	<i>C</i> ₁₁ (N/m)	<i>C</i> ₁₂ (N/m)	<i>C</i> ₂₂ (N/m)	<i>C</i> ₆₆ (N/m)
Cu ₂ O ₂	2.80	5.66	2.02	136.14	0.79	—	68.45	8.65	20.92	8.88
Cu ₂ S ₂	3.35	5.50	2.29	97.20	1.27	0.64	40.74	1.23	7.55	2.37
Cu ₂ Se ₂	3.54	5.41	2.65	87.34	1.11	0.6	38.27	-0.71	2.88	0.84

Ag ₂ O ₂	3.05	6.28	1.22	135.36	1.25	0.17	52.12	6.65	17.70	6.20
Ag ₂ S ₂	3.57	6.07	2.45	98.57	1.60	0.98	27.37	2.14	7.39	2.40
Ag ₂ Se ₂	3.76	6.05	2.76	91.03	1.27	0.86	22.70	0.94	4.73	1.28
Au ₂ O ₂	3.10	6.06	1.37	128.86	1.02	0.18	61.66	10.56	25.96	10.64
Au ₂ S ₂	3.54	6.26	2.26	105.6	2.19	1.35	41.26	4.10	13.05	5.40
Au ₂ Se ₂	3.72	6.34	2.55	99.26	1.79	1.21	34.56	2.70	9.23	3.37

2.2. Emerging NPR in R-Cu₂Se₂

Based on mechanical stability, mechanical properties of the R-X₂Y₂ monolayers are investigated. In-plane Poisson's ratio is obtained as follows³¹:

$$v(\theta) = \frac{C_{12}\sin^4\theta - B\sin^2\theta\cos^2\theta + C_{12}\cos^4\theta}{C_{11}\sin^4\theta - A\sin^2\theta\cos^2\theta + C_{22}\cos^4\theta} \quad (1)$$

where $A = (C_{12}C_{22} - C_{12}^2)/C_{66} - 2C_{12}$ and $B = C_{11} + C_{22} - (C_{12}C_{22} - C_{12}^2)/C_{66}$. Fig. 1(d) shows the maximum and minimum values of Poisson's ratio for R-TMCs. Compared with other R-X₂Y₂ binary compounds, R-Cu₂Se₂ has the widest Poisson's ratio range, which is between -0.3 and 0.6. Most interestingly, an emerging NPR is found in R-Cu₂Se₂ despite having a similar structure to other binary R-X₂Y₂. The embedding of Fig. 1(d) is the Poisson's ratio of R-Cu₂Se₂ as a function of angle θ . The Poisson's ratio is the smallest and negative along the 0 and 180 degree directions, while the largest positive Poisson's ratio occurs at $\sim 30^\circ$, $\sim 150^\circ$, $\sim 210^\circ$, and $\sim 330^\circ$ degrees. Monolayer R-Cu₂Se₂ exhibits a strong anisotropic NPR along the orthogonal direction. The high NPR of -0.27 comes from the y direction, which is higher than α -phosphorene (-0.027)²⁸, tetra-silicene (-0.055)³⁹, WN₄ (0.113)⁴⁰, penta-graphene (0.068)⁴¹ and Be₅C₂ (-0.16)⁴². In addition, the orthogonal anisotropic in-plane Poisson's ratio is rarely found in other anisotropic configurations, such as hinge-structures materials^{28,43}, and borophane³². Most importantly, this emerging NPR is independent of traditional re-entry mechanisms, since NPR behavior is not found in other R-X₂Y₂ monolayers. Such an effect cannot be intuitively explained geometrically and a similar phenomenon is reported in 1T-TMCs³⁵ due to the strong coupling between specific orbitals. The difference is that R-X₂Y₂ of the same main group has similar orbital hybridization, but only R-Cu₂Se₂ exhibits NPR behavior. The emerging NPR in R-Cu₂Se₂ is expected to provide new valuable clues for the regulation of electronic effects on NPR behavior.

2.3. Anisotropy of the NPR

Furthermore, orthogonal forced strains are applied in the x and y directions to reveal the anisotropic NPR behavior for R-Cu₂Se₂, respectively. The response of monolayer R-Cu₂Se₂'s lattice parameters to uniaxial strain is plotted in Fig. 2. The Poisson's ratio is defined as⁴⁴

$$v_1 = -\partial\varepsilon_1/\partial\varepsilon_2, \quad (2)$$

where ε_1 is the response strain driven by forced strain ε_2 . The intrinsic Poisson's ratio v_1 can be obtained by fitting $\varepsilon_1 = -v_1\varepsilon_2 + v_2\varepsilon_2^2 + v_3$. The behavior for a larger strain range (-6%-6%) is provided in Supplementary Fig. S3. Here, as shown in Fig. 2(a) and (b), the response lattice constant increases linearly with forced strain, indicating that the lattice expands when it is stretched, *i.e.*, NPR. The intrinsic Poisson's ratios in the y direction and x direction are -0.25 and -0.07, respectively, which are in good agreement with the results based on the elastic constant calculation. The primitive cell of monolayer R-Cu₂Se₂ contains two Cu atoms and two Se atoms, but the displacement mode of the two Se atoms is equivalent due to symmetry. Thus, the mechanical explanation of NPR can be understood by tracing the evolution of the tetrahedron composed of Cu₁, Cu₂ and Se₁ atoms as shown in Fig. 1(b) and Fig. 2(c, d). As shown in Fig. 2(c), a uniaxial forced strain will increase the distance between its adjacent Cu₁ and Cu₂ atoms, inducing the Se₁ atom to move downward when it is applied along the x direction. Critically, angle θ increases, contributing to NPR. Similarly, strain along the y direction induces the downward movement of Se₁ atoms as shown in Fig. 2(d), which causes the Cu₁ atoms to move to both sides of the x -axis, and eventually produces an NPR. The origin of anisotropic NPR lies geometrically in the flattening of the tetrahedron due to uniaxial strain.

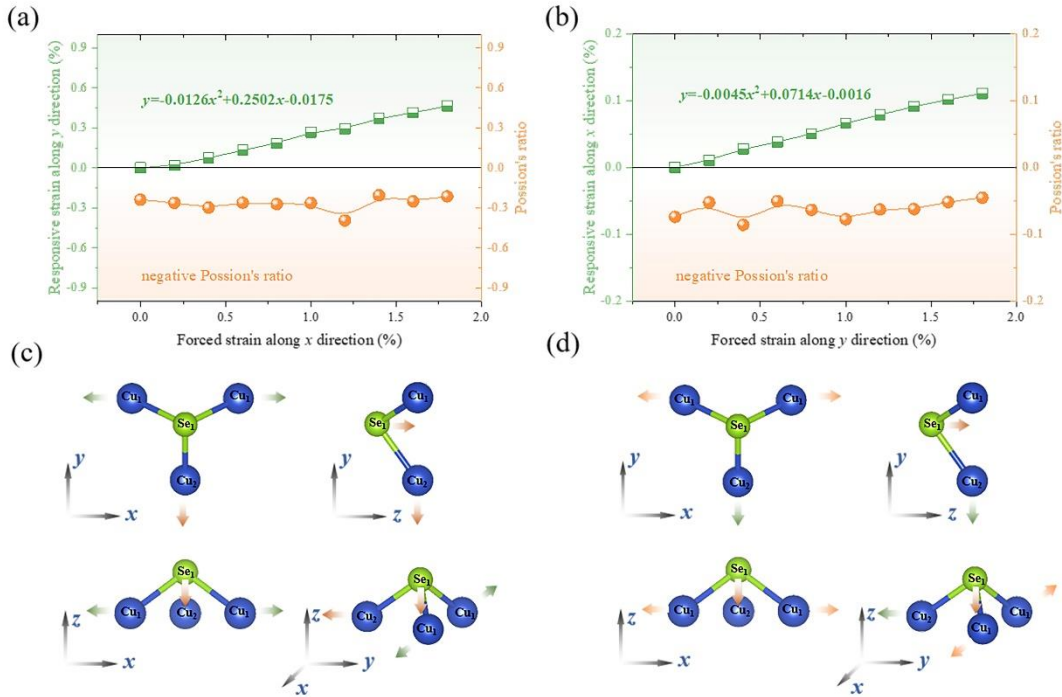


Figure 2. Mechanical response driven by strains along the (a) x and (b) y directions, respectively. The localized atomic displacements corresponding to the negative Poisson's ratio along the (c) x and (d) y directions, respectively. The green and red arrows indicate forced and responsive strain-driven atomic displacements, respectively.

2.4. The mechanism underlying NPR

Noticed, the geometric evolution is not sufficient to explain the emerging NPR, as only R-Cu₂Se₂ appears NPR but not in other R-X₂Y₂. To further explain such emerging NPR, we take the geometrical and electronic responses of monolayer R-Cu₂Se₂ and R-Ag₂Se₂ when strain is applied along the x -direction as an example. The geometric response along the y -axis is related to the projected length l of R-X₂Y₂ on the side, which further depends on the geometrical change of the lattice atoms on the projected triangle. Hence the key parameters are obtained, namely the feature lengths l_1 and l_2 and the feature angle θ . When tensile strain is applied, two competing geometric modes are extracted as shown in Fig. 3 (e): (1) geometrical length (GL) mode, where only the bond length shortens; (2) geometrical angle (GA) mode, meaning only the angle changes. The contributions of the two modes to the Poisson ratio are opposite and competing, *i.e.* the GA mode tends to have a NPR while the GL mode contributes a positive Poisson's ratio (PPR). Interestingly, the geometric responses of monolayer R-Cu₂Se₂ and R-Ag₂Se₂ exhibit a consistent behavior as shown in Fig. 3 (a) and (b), namely feature angle θ increases and feature lengths l_1 and l_2 decrease. Similar geometric evolution stems from their same geometric configuration and the same main group of elements. In geometric evolution, the emerging NPR originates from the GA mode (the increase of feature angle θ). The difference is that the angle θ increases faster with strain in monolayer R-Cu₂Se₂ compared to that in monolayer R-Ag₂Se₂, which overcomes the GL mode that tends to produce a PPR. Compared to other R-X₂Y₂, monolayer R-Cu₂Se₂ has relatively strong strain response of intralayer interactions due to the geometrically smallest characteristic angle θ as shown in Fig. 3(c). A smaller characteristic angle means it is more likely to produce an increase in response. This strong intralayer interaction response originates from the overlapping of wave functions within the layers, which can be visually reflected in the electron localization function (ELF) as shown in Fig. 3(f–i). When tensile strain is applied, the overlap of electron clouds between Se atoms in monolayer R-Cu₂Se₂ [Fig. 3(f) and (g)] is deepened while the overlap in R-Ag₂Se₂ is relatively weak [Fig. 3(h) and (i)], which leads to stronger lateral repulsion within the layer.

Thereby a stronger intralayer interaction response is found in R-Gu₂Se₂, which is reflected in the angle θ increasing faster (stronger GA mode). To quantify the strength of intralayer interaction response, the integrated Crystal Orbital Hamilton Population (ICOHP) between the X₁ and X₂ atoms is extracted as shown in Fig. 3(d). When the strain increases by 4%, the ICOHP of monolayer R-Cu₂Se₂ increases by more than 7%, which is significantly faster than that of monolayer R-Ag₂Se₂ (no more than 2%). Faster growth in the ICOHP means a stronger intralayer interaction response. Therefore, the strong intralayer response drives the faster increase of the characteristic angle θ in monolayer R-Cu₂Se₂, ultimately leading to structure-independent NPR behavior.

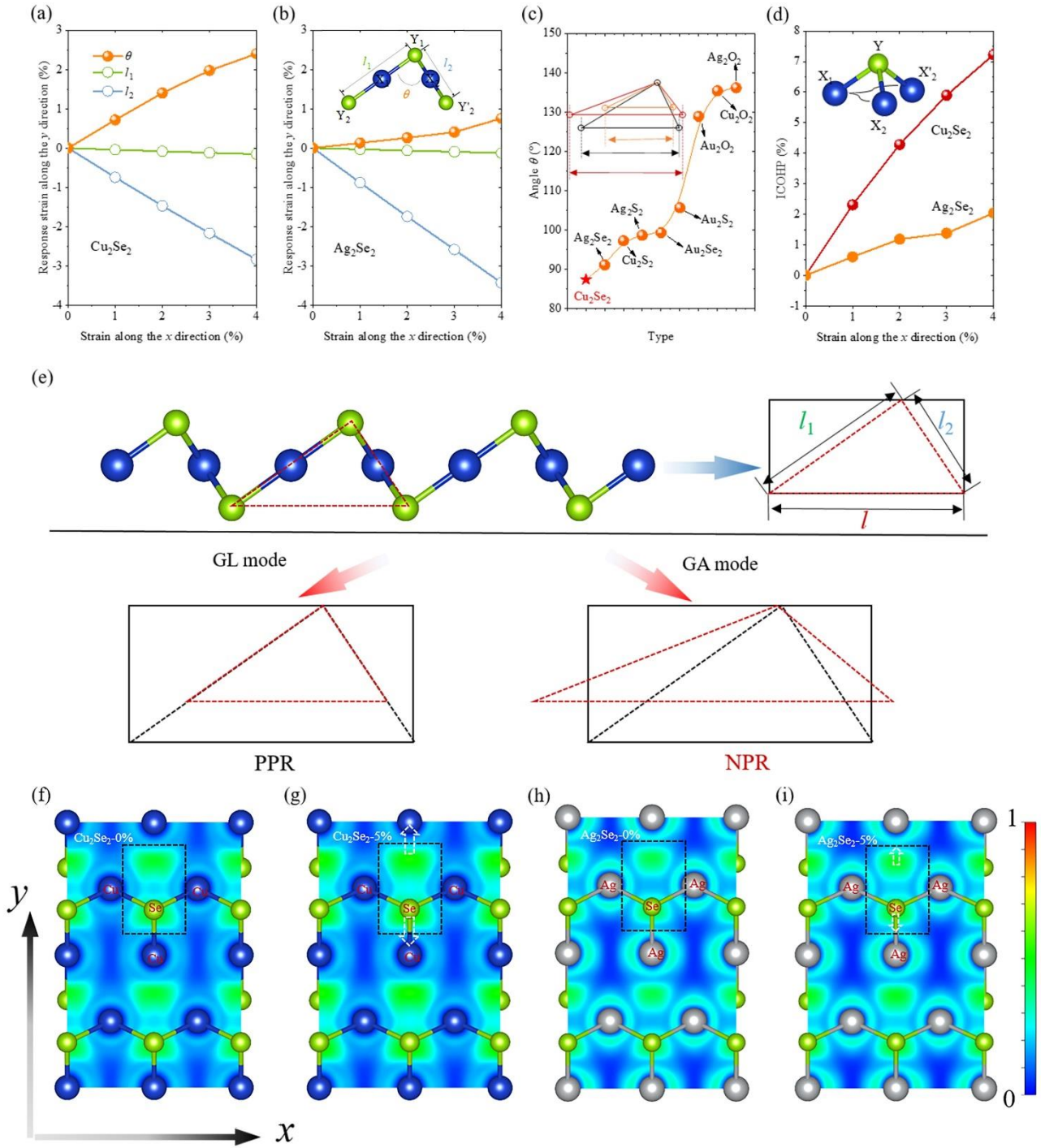


Figure 3. The origin of the NPR. Geometric response driven by strains along the x direction in (a) $R\text{-Cu}_2\text{Se}_2$ and (b) $R\text{-Ag}_2\text{Se}_2$. (c) Comparison of characteristic angles in $R\text{-X}_2\text{Y}_2$ with different components. (d) Contrast of changes in ICOHP with strain for $R\text{-Cu}_2\text{Se}_2$ and $R\text{-Ag}_2\text{Se}_2$. (e) Two competing modes in the evolution of NPR, including geometrical length (GL) and geometrical angle (GA) modes. (f, g) The electron localization function (ELF) of Cu_2Se_2 when the strain is (f) 0% and (g) 5%. (h, i) The ELF of Ag_2Se_2 when the strain is (h) 0% and (i) 5%.

2.5. Fundamental understanding of NPR from orbital evolution

To gain further insight into the emerging NPR in this novel X_2Y_2 -type R-TMCs monolayers, fundamental electronic properties of the $R-X_2Y_2$ monolayers need to be investigated. Further, the HSE06 functional is considered to obtain accurate band gap, which are higher than the results of the PBE functional as shown in Fig. 4(a) and Table. 1. Differently, all $R-X_2Y_2$ monolayers exhibit semiconducting characteristics based on the HSE06 functional. Among them, monolayer $R-Au_2S_2$ exhibits the largest band gap of 2.19 eV while the smallest band gap of monolayer $R-Cu_2O_2$. The HSE06-based band gap of the $R-X_2Y_2$ monolayers is in the range of 0.7 to 2.2 eV, which fits well within the ideal band gap (0.9-1.6 eV) for optical absorption as shown in the iridescent area in Fig. 4(a). Based on the HSE06 functional, monolayer $R-Cu_2Se_2$ exhibits an indirect band gap of 1.16 eV as a semiconductor. As shown in Fig. S6, $R-X_2Y_2$ monolayers have strong absorption peaks in the visible range of 1.62 eV~3.11 eV, which means that $R-X_2Y_2$ monolayers have outstanding phonon absorption ability. Besides, $R-X_2Y_2$ monolayers also have strong absorption peaks in the ultraviolet region (>3.11 eV), indicating their great potential in optical devices. More information can be provided in the supplementary Note S2 and Fig. S6. Combined with this emerging NPR, the promised electrical and optical properties enable $R-X_2Y_2$ to meet functional requirements for practical applications.

Further, the orbital evolution of $R-Cu_2Se_2$ is plotted in Fig. 4(b) to demonstrate fundamental understanding for emerging NPR. The valence band maximum (VBM) is located between the high symmetry point path S-Y, and the conduction band minimum (CBM) is located between Γ -X. Fig. 4(c) shows the 3D images of VBM and CBM. The conduction band with the lowest energy forms two valley peaks (C_1 and C_2) with a little energy difference of 0.19 eV, which are located in the Γ -X and S-Y paths respectively. Meanwhile, the VBM along S-Y exhibits a quasi-flat energy band, forming a quasi-direct band gap of 1.35 eV. The quasi-flat band leads to a sharp peak in partial density of states ($pDOS$). The VBM are mainly contributed by Se- p , Cu- p and Cu- d orbitals while the CBM is dominated by Se- p and Cu- d orbitals. In the entire bonding region, the contribution of Se- p and Cu- d orbitals is much higher than that of other orbitals. Noted that the energy of the s electron in the Se atom is much lower than the bonding electrons than Cu atom, forming a lone pair of electrons as shown in the inset in the lower right corner of Fig. 4(b). The weak sp^3 hybridization is captured and further hybridized with the d orbital to produce a more complex multi-orbital effect. Hence, the Se atoms in the pyramidal coordination

center form complex multi-orbital hybridizations during NPR evolution, which are more likely to promote smaller bond angles than simple sp or sp^2 hybridizations. In addition, the electron cloud of the lone pair s electrons in the central Se atom is hypertrophic, which has a large repulsive force for the bonding electron pair. Thus, the lone pair s electrons can make the bonding electron pair closer to each other, and the bond angle is compressed and becomes smaller. Furthermore, the central Se atom has a smaller electronegativity of 2.55 compared to 2.58 and 3.44 for the O and S atoms. Hence, the bonding electron is farther away from the Se atom, the repulsion between the bonding electron pair becomes smaller, and the bond angle becomes smaller. The lone pair s electrons and weak electronegativity in Se atoms can be intuitively revealed through the petal-shaped electron cloud in the ELF shown in Fig. 3 (d) and (e). The strong lone-pair electrons and weak electronegativity of Se atom leads to a smaller characteristic angle of R-Cu₂Se₂ [Fig. 3(c)]. Thus, when subjected to tensile strain, the GA mode is easier to respond [Fig. 3(a)] and the stronger intralayer interaction response [Fig. 3(d)] can be captured, ultimately contributing to the unique NPR behavior.

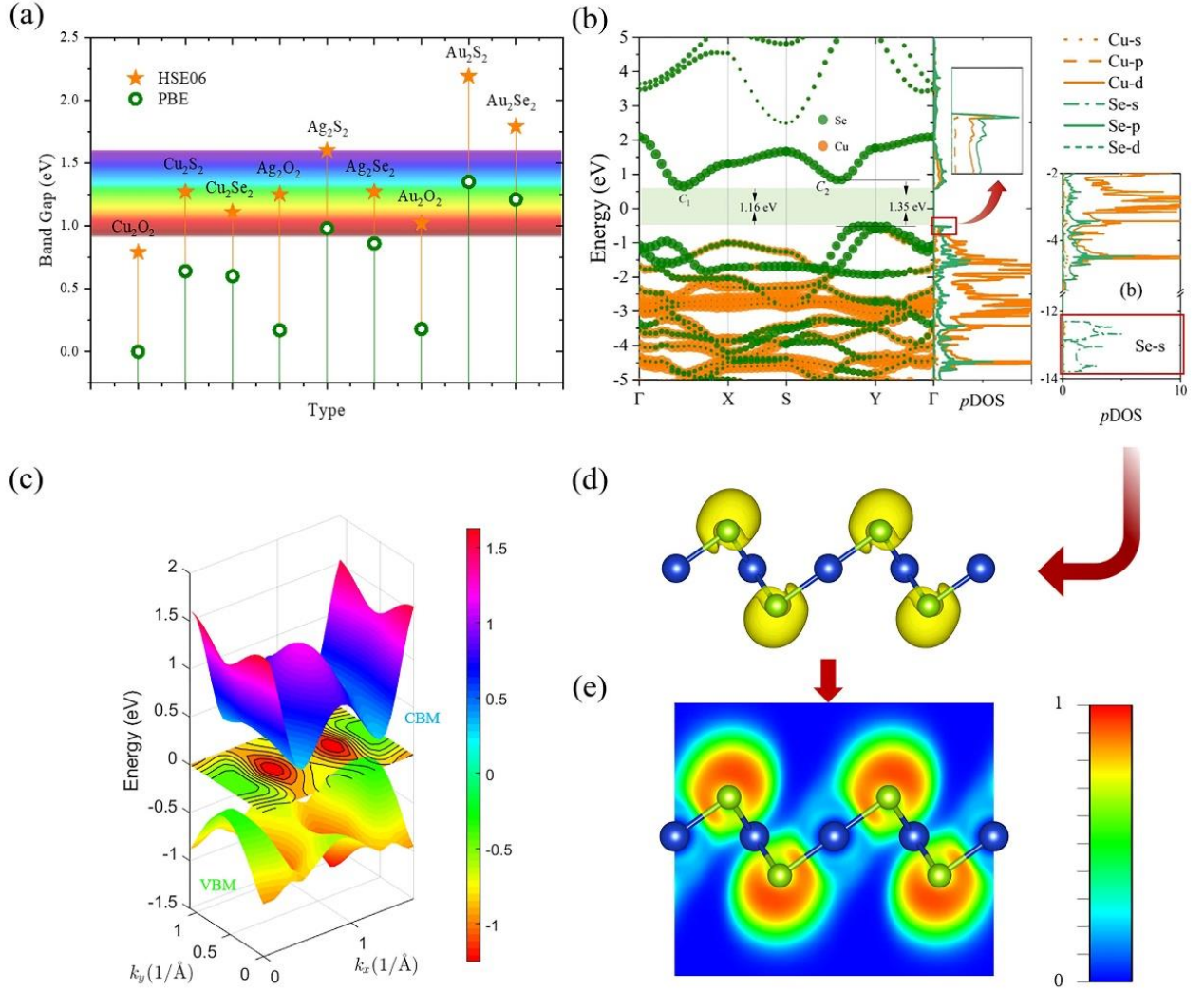


Figure 4. Electronic properties of $R-X_2Y_2$ ($X=Cu, Ag, Au$; $Y=O, S, Se$) monolayers. (a) The band gaps of the $R-X_2Y_2$ monolayers from the HSE06 and PBE functionals. The rainbow band means the ideal optical absorption band gap. (b) The energy band structure of monolayer $R-Ce_2Se_2$. (c) The 3D CBM and VBM of monolayer $R-Ce_2Se_2$. (d) 3D electron localization function (ELF) for monolayer $R-Ce_2Se_2$ (isosurface of 0.8). (e) 2D electron localization function of monolayer $R-Ce_2Se_2$.

3. Conclusion

In summary, we have proposed a novel 2D TMCs (R-TMCs) with NPR and performed a comprehensive investigation of the Poisson's ratio behavior in X_2Y_2 -type ($X=Cu, Ag, Au$ and $Y=O, S, Se$) rectangular TMCs monolayers. When strain is applied, only monolayer $R-Cu_2Se_2$ has an intrinsic NPR behavior. Unlike the previously reported re-entry mechanism-dominated NPR behavior, this behavior can be attributed to a strong

strain response of intralayer interaction driven by electronic effects. Insights into the origin of NPR can be obtained to trace key parameters (length l_1 , l_2 and angle θ) in geometric evolution, which can be further explained by the response of two competing modes: GA mode (dominated by angle θ) and GL mode (dominated by length l_1 , l_2). All R-X₂Y₂ monolayers exhibit the same evolutionary path, but the response strength of R-Cu₂Se₂ is stronger due to the smaller angle θ . The strong intralayer interaction response originates from the lateral repulsive forces generated by the accumulated intralayer charges, and is further quantified by ELF and ICOHP, which can be further traced to the lone pair electrons and weak electronegativity of Se atoms under multi-orbital hybridization. The understanding of this unique NPR mechanism can provide valuable clues and guidance for the discovery or design of novel auxetic materials. To our knowledge, such NPR behavior has not been reported in other copper selenide phases, although there is ubiquitous copper compounds in nature's abundant mineral resources or even copper selenides in different dimensions have been synthesized experimentally. Combining the promising electrical and optical properties, the unique auxetic properties enable monolayer R-Cu₂Se₂ to lead to multi-functionality.

4. Computational Details

All first-principles calculations are performed based on density functional theory (DFT) utilizing the Vienna *ab-initio* simulation package (VASP)⁴⁵. Based on the Perdew–Burke–Ernzerhof (PBE)⁴⁶ functional, the kinetic energy cutoff of 740 eV and a Monkhorst-Pack⁴⁷ q -mesh of 21×14×1 are used for structural optimization until the energy accuracy of 10⁻⁶ eV and the Hellmann-Feynman force accuracy of 10⁻³ eV/Å. Phonon dispersion is calculated by constructing a 6×4×1 supercell with a 2×2×1 q -mesh based on the finite displacement difference method as implemented in *PHONOPY*⁴⁸. The calculation of the elastic constant is based on the energy-strain method using *VASPKIT*⁴⁹. The accurate energy band gap and optical properties are based on the hybrid HSE06 functional^{50,51}.

ACKNOWLEDGEMENTS

This work is supported by the National Natural Science Foundation of China (Grant Nos. 52006057, 51906097, and 11904324), the Fundamental Research Funds for the Central Universities (Grant Nos. 531119200237 and 541109010001), and the State Key Laboratory of Advanced Design and Manufacturing for

Vehicle Body at Hunan University (Grant No. 52175013). The numerical calculations in this paper have been done on the supercomputing system of the National Supercomputing Center in Changsha.

AUTHOR CONTRIBUTIONS

G.Q. supervised the project. *L.Y.* performed all the calculations and analysis. All the authors contributed to interpreting the results. The manuscript was written by *L.Y.* with contributions from all the authors.

References

1. Lipsett, A. W. & Beltzer, A. I. Reexamination of dynamic problems of elasticity for negative Poisson's ratio. *The Journal of the Acoustical Society of America* **84**, 2179–2186 (1988).
2. Park, Y. J. & Kim, J. K. The effect of negative Poisson's ratio polyurethane scaffolds for articular cartilage tissue engineering applications. *Advances in Materials Science and Engineering* **2013**, undefined-undefined (2013).
3. Evans, K. E. & Alderson, A. Auxetic Materials: Functional Materials and Structures from Lateral Thinking! *Advanced Materials* **12**, 617–628 (2000).
4. Scarpa, F. Auxetic materials for bioprotheses [In the Spotlight]. *IEEE Signal Processing Magazine* **25**, 128–126 (2008).
5. Jiang, J.-W., Kim, S. Y. & Park, H. S. Auxetic nanomaterials: Recent progress and future development. *Applied Physics Reviews* **3**, 041101 (2016).
6. Yang, W., Li, Z.-M., Shi, W., Xie, B.-H. & Yang, M.-B. Review on auxetic materials. *Journal of Materials Science* **39**, 3269–3279 (2004).
7. Gn, G., Al, G., Rs, L. & T, R. Poisson's ratio and modern materials. *Nature materials* vol. 10 <https://pubmed.ncbi.nlm.nih.gov/22020006/> (2011).

8. Baughman, R. H., Shacklette, J. M., Zakhidov, A. A. & Stafström, S. Negative Poisson's ratios as a common feature of cubic metals. *Nature* **392**, 362–365 (1998).
9. Phys. Rev. B 19, 2030 (1979) - Existence of a negative Poisson ratio in fcc crystals.
<https://webvpn.hnu.edu.cn/https/77726476706e69737468656265737421faf8548e29316443300999bfd65a3132/prb/abstract/10.1103/PhysRevB.19.2030>.
10. Özdamar, B. *et al.* Structural, vibrational, and electronic properties of single-layer hexagonal crystals of group IV and V elements. *Phys. Rev. B* **98**, 045431 (2018).
11. Peng, B. *et al.* The conflicting role of buckled structure in phonon transport of 2D group-IV and group-V materials. *Nanoscale* **9**, 7397–7407 (2017).
12. Yu, L. *et al.* Abnormal enhancement of thermal conductivity by planar structure: A comparative study of graphene-like materials. *International Journal of Thermal Sciences* **174**, 107438 (2022).
13. Wang, H. *et al.* Intrinsically low lattice thermal conductivity of monolayer hexagonal aluminum nitride (h-AlN) from first-principles: A comparative study with graphene. *International Journal of Thermal Sciences* **162**, 106772 (2021).
14. Zhou, J. *et al.* A library of atomically thin metal chalcogenides. *Nature* **556**, 355–359 (2018).
15. Chen, X., Wang, D., Liu, X., Li, L. & Sanyal, B. Two-Dimensional Square-A₂B (A = Cu, Ag, Au, and B = S, Se): Auxetic Semiconductors with High Carrier Mobilities and Unusually Low Lattice Thermal Conductivities. *J. Phys. Chem. Lett.* **11**, 2925–2933 (2020).
16. Yu, L., Yan, Q. & Ruzsinszky, A. Negative Poisson's ratio in 1T-type crystalline two-dimensional transition metal dichalcogenides. *Nat Commun* **8**, 15224 (2017).

17. Huang, C. *et al.* Prediction of intrinsic ferromagnetic ferroelectricity in a transition-metal halide monolayer. *Physical review letters* **120**, 147601 (2018).
18. Rosales, B. A. *et al.* Reversible multicolor chromism in layered formamidinium metal halide perovskites. *Nature communications* **11**, 1–12 (2020).
19. Lin, Y. *et al.* Metallic surface doping of metal halide perovskites. *Nature communications* **12**, 1–8 (2021).
20. Yu, L., Qin, Z., Wang, H., Zheng, X. & Qin, G. *Half-Negative Poisson's Ratio in Graphene+ With Intrinsic Dirac Cone: A Competitor to Graphene?*
<https://papers.ssrn.com/abstract=3976476> (2021) doi:10.2139/ssrn.3976476.
21. Ma, F. *et al.* Half-Auxeticity and Anisotropic Transport in Pd Decorated Two-Dimensional Boron Sheets. *Nano Lett.* **21**, 2356–2362 (2021).
22. Qin, Z., Qin, G. & Hu, M. Origin of anisotropic negative Poisson's ratio in graphene. *Nanoscale* **10**, 10365–10370 (2018).
23. Qin, G. Negative Poisson's ratio in two-dimensional honeycomb structures. *npj Computational Materials* **6** (2020).
24. Wang, Y. *et al.* The consistent behavior of negative Poisson's ratio with interlayer interactions. *Mater. Adv.* 10.1039/D2MA00118G (2022) doi:10.1039/D2MA00118G.
25. Wan, J., Jiang, J.-W. & S. Park, H. Negative Poisson's ratio in graphene oxide. *Nanoscale* **9**, 4007–4012 (2017).
26. Grima, J. *et al.* Tailoring Graphene to Achieve Negative Poisson's Ratio Properties. *Advanced Materials* **27**, (2014).

27. Jiang, J.-W. & Park, H. S. Negative Poisson's Ratio in Single-Layer Graphene Ribbons. *Nano Lett.* **16**, 2657–2662 (2016).
28. Jiang, J.-W. & Park, H. S. Negative poisson's ratio in single-layer black phosphorus. *Nat Commun* **5**, 4727 (2014).
29. Liu, B. *et al.* Negative Poisson's ratio in puckered two-dimensional materials. *Phys. Rev. Materials* **3**, 054002 (2019).
30. Pan, J. *et al.* Auxetic two-dimensional transition metal selenides and halides. *npj Comput Mater* **6**, 154 (2020).
31. Peng, R. *et al.* Single-Layer Ag₂S: A Two-Dimensional Bidirectional Auxetic Semiconductor. *Nano Lett.* **19**, 1227–1233 (2019).
32. Kou, L. *et al.* Auxetic and Ferroelastic Borophane: A Novel 2D Material with Negative Poisson's Ratio and Switchable Dirac Transport Channels. *Nano Lett.* **16**, 7910–7914 (2016).
33. Jiang, J.-W. & Park, H. S. Negative Poisson's Ratio in Single-Layer Graphene Ribbons. *Nano Lett.* **16**, 2657–2662 (2016).
34. Ma, Z. *et al.* Multiferroicity and giant in-plane negative Poisson's ratio in wurtzite monolayers. *npj Comput Mater* **8**, 51 (2022).
35. Yu, L., Yan, Q. & Ruzsinszky, A. Negative Poisson's ratio in 1T-type crystalline two-dimensional transition metal dichalcogenides. *Nat Commun* **8**, 15224 (2017).
36. Sokolov, I. O. *et al.* Microcanonical and finite-temperature *ab initio* molecular dynamics simulations on quantum computers. *Phys. Rev. Research* **3**, 013125 (2021).

37. Sanchez, J., Fulla, J., Andrade, M. C. & de Andres, P. L. *Ab initio* molecular dynamics simulation of hydrogen diffusion in α -iron. *Phys. Rev. B* **81**, 132102 (2010).
38. Wu, Z. *et al.* Crystal structures and elastic properties of superhard Ir N₂ and Ir N₃ from first principles. *Phys. Rev. B* **76**, 054115 (2007).
39. Qiao, M., Wang, Y., Li, Y. & Chen, Z. Tetra-silicene: a semiconducting allotrope of silicene with negative Poisson's ratios. *The Journal of Physical Chemistry C* **121**, 9627–9633 (2017).
40. Jin, W., Sun, W., Kuang, X., Lu, C. & Kou, L. Negative Poisson Ratio in Two-Dimensional Tungsten Nitride: Synergistic Effect from Electronic and Structural Properties. *J. Phys. Chem. Lett.* **11**, 9643–9648 (2020).
41. Zhang, S. *et al.* Penta-graphene: A new carbon allotrope. *Proc Natl Acad Sci USA* **112**, 2372–2377 (2015).
42. Wang, Y., Li, F., Li, Y. & Chen, Z. Semi-metallic Be₅C₂ monolayer global minimum with quasi-planar pentacoordinate carbons and negative Poisson's ratio. *Nat Commun* **7**, 11488 (2016).
43. Kong, X. *et al.* Tunable auxetic properties in group-IV monochalcogenide monolayers. *Phys. Rev. B* **98**, 184104 (2018).
44. Qin, G. & Qin, Z. Negative Poisson's ratio in two-dimensional honeycomb structures. *npj Comput Mater* **6**, 51 (2020).
45. Kresse, G. & Hafner, J. *Ab initio* molecular-dynamics simulation of the liquid-metal–amorphous-semiconductor transition in germanium. *Phys. Rev. B* **49**, 14251–14269 (1994).

46. Perdew, J. P., Burke, K. & Ernzerhof, M. Generalized Gradient Approximation Made Simple. *Phys. Rev. Lett.* **77**, 3865–3868 (1996).
47. Monkhorst, H. J. & Pack, J. D. Special points for Brillouin-zone integrations. *Phys. Rev. B* **13**, 5188–5192 (1976).
48. Chaput, L., Togo, A., Tanaka, I. & Hug, G. Phonon-phonon interactions in transition metals. *Phys. Rev. B* **84**, 094302 (2011).
49. Wang, V., Xu, N., Liu, J.-C., Tang, G. & Geng, W.-T. VASPKIT: A user-friendly interface facilitating high-throughput computing and analysis using VASP code. *Computer Physics Communications* 108033 (2021) doi:10.1016/j.cpc.2021.108033.
50. Śpiewak, P. & Kurzydłowski, K. J. Formation and migration energies of the vacancy in Si calculated using the HSE06 range-separated hybrid functional. *Phys. Rev. B* **88**, 195204 (2013).
51. Deák, P., Aradi, B., Frauenheim, T., Janzén, E. & Gali, A. Accurate defect levels obtained from the HSE06 range-separated hybrid functional. *Phys. Rev. B* **81**, 153203 (2010).